A COMPARISON OF THEORY AND EXPERIMENT FOR COUPLED ROTOR BODY STABILITY OF A BEARINGLESS ROTOR MODEL IN HOVER AND FORWARD FLIGHT

Paul H. Mirick*
U.S. Army Aerostructures Directorate, Hampton, Virginia

Abstract

Seven cases were selected for correlation from a 1/5.86 Froude-scale experiment that examined several rotor designs which were being considered for full-scale flight testing as part of the Bearingless Main Rotor (BMR) program. The model rotor hub used in these tests consisted of back-to-back C-beams as flexbeam elements with a torque tube for pitch control. The first four cases selected from the experiment were hover tests which examined the effects on rotor stability of variations in hub-to-flexbeam coning, hub-to-flexbeam pitch, flexbeam-to-blade coning, and flexbeam-to-blade pitch. The final three cases were selected from the forward flight tests of the optimum rotor configuration as defined during the hover test. The selected cases examined the effects of variations in forward speed, rotor speed, and shaft angle. Analytical results from Bell Helicopter Textron, Boeing Vertol, Sikorsky Aircraft, and the U.S. Army Aeromechanics Laboratory were compared with the data and the correlations ranged from poor-to-fair to fair-to-good.

Introduction

As part of the Methodology Assessment, seven cases were selected from the experiments reported in Ref. 1 for comparison with theoretical models. The experiment reported in Ref. 1 was conducted by the Boeing Vertol Company as part of the U.S. Army Applied Technology Laboratory program to design, fabricate, and demonstrate by flight test the feasibility of a Bearingless Main Rotor (BMR). This experiment included both hover and forward flight testing of a 1/5.86 Froude-scale model bearingless rotor. From the extensive data on a coupled rotor/body stability that was generated, four hover test cases and three forward flight cases were selected for comparison. The cases were chosen to determine the ability of the analyses to model a bearingless rotor with differences in precone, blade droop, and flexbeam twist in hover; and to model the effects of thrust, shaft angle, airspeed, and rotor speed in forward flight.

The theoretical models compared with the data included the Bell Helicopter Textron DRAV21 analysis in hover and C81 in forward flight, the Boeing Vertol C-90 code, two versions of the Sikorsky E-927 analysis, the Sikorsky G400 code, and the U.S. Army Aeromechanics Laboratory FLAIR analysis.

This paper briefly describes the experiment from which these data were obtained and presents the correlation. Conclusions are presented as to the quality of the agreement between theory and experiment. Appendices document the experimental model properties, tabulate the experimental data points, and show all of the correlations.

Description of Experiment

As part of the U.S. Army Applied Technology Laboratory program to design, fabricate, and demonstrate by flight test the feasibility of a Bearingless Main Rotor (BMR), the Boeing Vertol Company conducted 1/5.86 Froude-scale tests of several candidate BMR configurations (Ref. 1). The testing included both hover and forward flight conditions. The hover tests were conducted to define the optimum model configuration for maximum air-resonance-mode damping. Configuration parameters which were varied to determine the optimum rotor included precone angle, blade sweep, blade first-chord frequency, and built-in pitch orientation of the root end C-beams. The optimum configuration was then tested in the Boeing Vertol wind tunnel at forward speeds up to a scale speed of 135 knots. The conditions simulated included level flight, banked turns, and climb-and-descents. This test provided an extensive data base on coupled rotor/body stability from which four hover- and three forward-flight cases were selected for correlation.

Model Description

The model used for this test is shown in Fig. 1. It consisted of a Froude-scale model rotor mounted on a rigid fuselage having pitch and roll degrees of freedom relative to the pedestal mounting. The complete model, including the drive motor and transmission, was mounted on a two-axis gimbal with ±7° pitch and ±9° roll. The model rotor diameter was 5.5 ft. A proportional (closed loop) control system equipped with a cyclic stick provided lateral and longitudinal control to fly the model in the pitch-and-roll degrees of freedom. In addition, a shaker system was installed in the cyclic control so that excitation of the model could be applied through the swashplate actuator at desired frequencies. Blade collective pitch was remotely controlled and was set initially by means of an open loop control and a pitch angle indicator. Other controls included the pedestal-mount pitch attitude, the stick trim,

*Aerospace Engineer.

and a variable incidence horizontal stabilizer to assist the operator in trimming the model in various flight conditions. Quick-acting and slow-acting (self-centering) snubbers were installed to arrest the fuselage motion divergences or to lock out body pitch-and-roll degrees of freedom. Rotor speed was controlled by the tunnel or test cell operator.

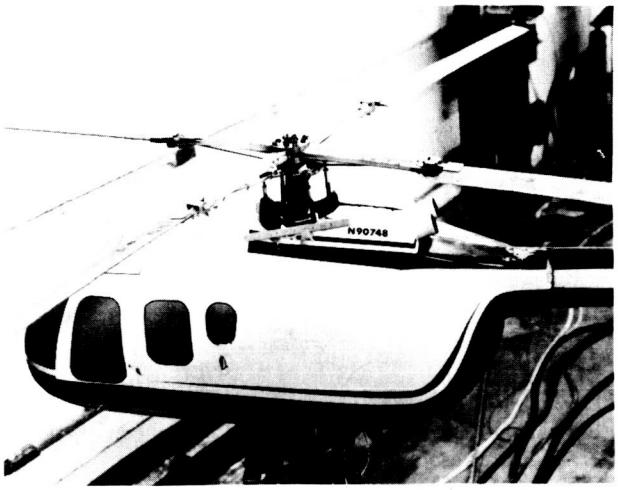

Fig. 1 1/5.86 Froude Scale Model.

Model power was supplied by a nine-horsepower water-cooled electric motor (rated at 10,000 rpm) through a 2.25:1 spur-gear reduction and then finally to the shaft through a 3:1 bevel-gear reduction.

The swashplate control system was mounted on the integral motor transmission assembly which is supported, through shear-force measuring devices, by roll pivots at the fore and aft ends of a rectangular gimbal frame. Adjustable pitch pivots on the sides of the frame provided the pitch degree of freedom and allowed variation in the center of gravity relative to the shaft axis. The model gimbal was supported through a vertical Y-frame to the pedestal base. A geometrically representative fuselage shell model of a balsa/fiberglass sandwich was suspended from the fore and aft ends of the transmission. The horizontal stabilizer was hand-adjustable in incidence.

The hub consisted of four beams made of 30% glass-filled nylon. This material was chosen to maintain geometric and aeromechanical similarity. Figure 2 shows the major components of the model hub. To study the effects of parameters variations, the hub was designed to allow beam-to-hub attachment angles of -6, 0, +6, +12° in pitch, and 0 and 2.5° in coning. The beam-to-blade juncture was designed to allow -12, -1.4, +3.6, +9.6, and +15.6° in pitch; 0 and -2.5° in blade sweep; and 0 and 2.5° in precone (negative droop).

The blade was constructed of a 1/8-in. diameter steel spar surrounded by a fiberglass-covered balsa airfoil. The blade-pitching mass moment of

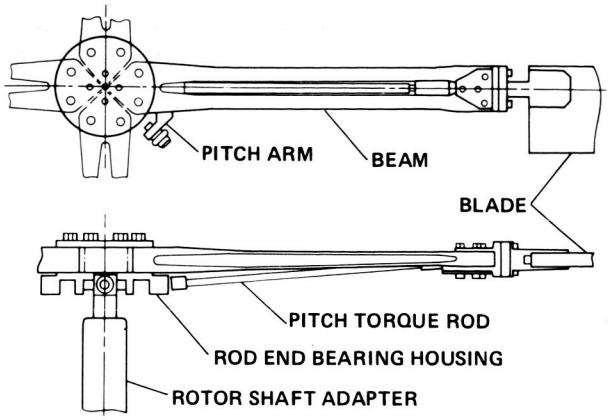

Fig. 2 Major components of BMR Froude Scale-Model Hub.

inertia together with the weight and chordwise balance was achieved through discrete distribution of tantalum wire slugs inside the balsa.

Deviations to the BO 105 blade design include exclusion of a tip overbalance weight, zero twist, and a NACA 21012 airfoil with a 1.65-in. chord and an additional trailing-edge tab of 0.17 in. over the full span of the blade. This makes a total chord of 1.82 in., which is 1/5.86-scale of the BO 105/BMR blade.

Test Procedure

The basic test procedure was to set up the desired test condition (e.g., rpm, tunnel speed, and collective pitch) and then trim the model. Trim attitude was held with the help of an SCAS system. The swashplate was oscillated in the lateral control direction for hover testing or in the longitudinal control direction for forward flight testing using a shaker set at a frequency of $(\Omega - \omega_\zeta)$. The shaker was then turned off, the transient response recorded, and the system modal damping determined by manual calculation and computer analysis.

Test Results

The model configuration was varied during the hover tests to define an optimum aeroelastically stable rotor configuration. This investigation concentrated on two aspects: 1) placing the instability boundary outside the helicopter operating rotor speed range, and 2) improving overall air resonance modal damping ratios near the normal operating rotor speed. Table 1 summarizes the configurations tested. Configuration I was selected as the baseline for the forward-flight wind tunnel testing. However, after a period of testing, it was observed that the air-resonance-damping mode had significantly increased. It was determined that the material properties of the glass-impregnated nylon had changed during testing

Table 1 BMR 1/5.86 Froude Sale Model Hover Test Configurations

Configuration	Hub-to-flexbeam pitch angle, θ_{fh}, deg[a]	Flexbeam-to-blade pitch angle, θ_{bf}, deg[a]	Flexbeam precone, β_{pc}, deg[b]	Blade droop, β_d, deg[c]	Blade sweep, Λ, deg[d]	Lead-lag dimensionless frequency @ 1028 rpm, ω_ζ
A	0	9.6	0.0	-2.5	0.0	0.68
B	-6	9.6	0.0	-2.5	0.0	0.68
C	+6	9.6	0.0	-2.5	0.0	0.68
D	-6	15.6	0.0	-2.5	0.0	0.68
E	0	9.6	2.5	0	0.0	0.68
F	+6	3.6	0.0	-2.5	0.0	0.68
G	+12	-2.4	0.0	-2.5	0.0	0.68
H	+12	-2.4	0.0	-2.5	-2.5	0.68
I	+12	-2.4	0.0	-2.5	0.0	0.65

[a]Positive, nose up.
[b]Positive, beam up.
[c]Positive, blade down.
[d]Positive, blade forward.

and therefore the Configuration I beams were replaced with the Configuration G beams.

Forward speed tests were conducted for the following conditions:

a) Airspeed sweeps in level flight at 1.0-G thrust from hover to a scaled 135 knots,

b) Thrust sweeps representing banked-turn load factors,

c) Climb and descent conditions at 1.0-G thrust,

d) Rotor speed variations, and

e) Shaft angle variations.

Selection of Test Cases

For the Methodology Assessment, seven cases from the 1/5.86 Froude-scale test were selected for correlation with the analyses. Table 2 provides the parameter varation for the cases along with the independent variables tested. Cases 1 through 4 are hover cases while 5 through 7 are for forward flight.

Case 1 was selected since it is essentially an uncoupled rotor and it should be the simplest to model mathematically. Case 2 was chosen because it has a region of neutral stability from about 900 to 1000 rpm and would provide some data on the sensitivity of the analyses in modeling this region. Case 3 was chosen to demonstrate the ability of the analyses to account for the effects of the combination of negative droop and pretwist which had shown the highest damping in the test program. Case 4 was selected to look at the effects of thrust as the independent variable. The three forward flight conditions comprise or make up the same configuration as for Cases 3 and 4. The forward flight conditions were selected to demonstrate the ability to model effects of airspeed (Case 5), shaft angle and inflow (Case 6), and rotor speed (Case 7). For Case 6, which shows the effect of climb and descent, the airspeed was selected that was the least stable for the regressing lead-lag mode. The same airspeed was used for Case 7 as well.

Correlation

The four hover cases were modeled using the Bell Helicopter Textron DRAV21 analysis, the Boeing Vertol C-90 code, the Sikorsky E927-3 Analysis, and the U.S. Army Aeromechanics Laboratory FLAIR code. The math model predictions and the experimental results for the four cases are compared in Figs. 3 through 6. Overall the DRAV21 code shows the best agreement between the experimental results and predictions.

The comparison of the predicted and measured lead-lag regressing mode damping as a function of rotor speed for Case 1 is presented in Fig. 3. The DRAV21 prediction (BH) shows fair-to-good agreement with the experimental results (shaded area). It accurately predicts the rotor speed stability boundary and closely predicts the level of damping. This analysis was performed without dynamic inflow; the same case with dynamic inflow shows only slight differences. Dynamic inflow was included in the subsequent comparisons.

The C-90 analysis (BV) closely predicts the rotor speed stability boundary and matches the trend of the experimental data, but predicts modal damping significantly higher than the test values; the agreement here is considered poor-to-fair. The reason for this is not known. However, a possible explanation is that Y-71, which provides the coupled mode shapes for the Y-71/C-60/C-90 family of programs, is not able to properly model the multiple load paths of the BMR dual-flexbeam and

Table 2 Selected Test Cases for Methodology Assessment

Case	Flexbeam precone, β_{pc}, deg	Hub-to-flexbeam pitch angle, θ_{fh}, deg	Blade droop, β_d, deg	Flexbeam-to-blade pitch angle, θ_{bf}, deg	Independent Variable
1	0	0	-2.5	-9.6	Ω varied, const thrust
2	2.5	0	0	9.6	Ω varied, const thrust
3	0	12	-2.5	-2.4	Ω varied, const thrust
4	0	12	-2.5	-2.4	thrust varied, const Ω
5	0	12	-2.5	-2.4	airspeed varied, const thrust
6	0	12	-2.5	-2.4	α_s varied, const. airspeed
7	0	12	-2.5	-2.4	Ω varied, const airspeed

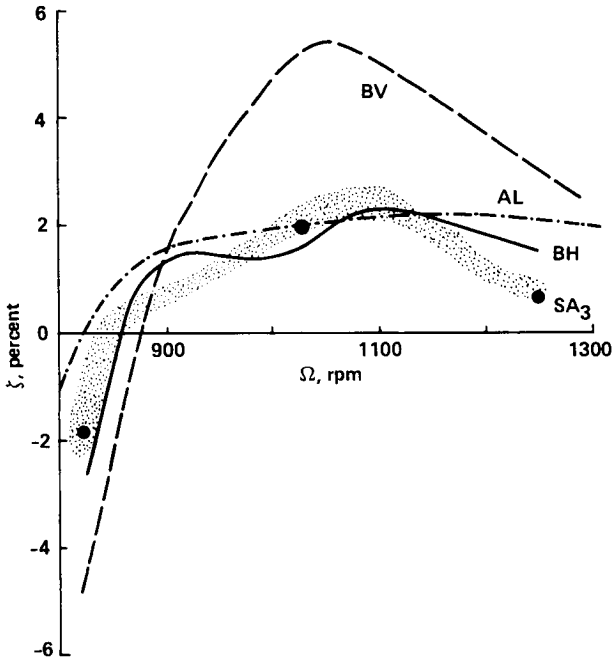

Fig. 3 Composite comparison of theory and experiment for Case 1, regressing lead-lag mode damping as a function of rotor speed for 1 g thrust; $\theta_{fh} = 0°$, $\theta_{bf} = 9.6°$, $\beta_{pc} = 0°$, $\beta_d = -2.5°$.

torque-tube design. Program Y-71 represents the dual flexbeam with a single beam approximation.

Sikorsky attempted to use both their G400 and E927-2 programs for this case, but were unable to obtain converged solutions. It was at this point that Sikorsky reintroduced torsion-bending coupling terms to the E927-2 analysis (that had been removed in the evolution of E927-1 to E927-2) to create the E927-3 version. Using this program (SA_3) three predicted values were obtained as shown by the circles. Although these three predicted points show excellent agreement with the data, the lack of additional predictions resulted in the correlation being judged as only fair.

The predictions made using the U.S. Army Aeromechanics Laboratory FLAIR model (AL) shows poor-to-fair agreement with the experimental data. The analysis slightly underpredicts the stability boundary and does not follow the decrease in stability shown in the experimental data above 1100 rpm.

Figure 4 presents the comparison of the predicted results with the experimental rotor data for Case 2. Both the DRAV21 and C-90 predicted the rotor speed stability boundary and showed good agreement with experimental data above 1050 rpm. However, these analyses fail to predict the region of neutral stability between 900 and 1000 rpm and overall are considered to show fair-to-good correlation. The E927-3 predictions are off scale and the correlation is very poor. The FLAIR analysis fails to predict the configuration as being stable and is judged poor.

Figure 5 shows the results of the comparison of the analysis with the experimental data of Case 3. Both the C-90 and DRAV21 codes predict the stability boundary while the FLAIR analysis underpredicts this boundary by about 100 rpm. The DRAV21 analysis shows fair-to-good agreement with the experimentally measured damping while the FLAIR and C-90 codes substantially overpredict the damping, so are considered poor. There are two sets of Sikorsky data for this case. The first set, SA_3 (shown as circles), are the results obtained using the E927-3 computer program. As with Case 1, these results show good agreement with the experimental data, but were judged only fair, in part because too few points were

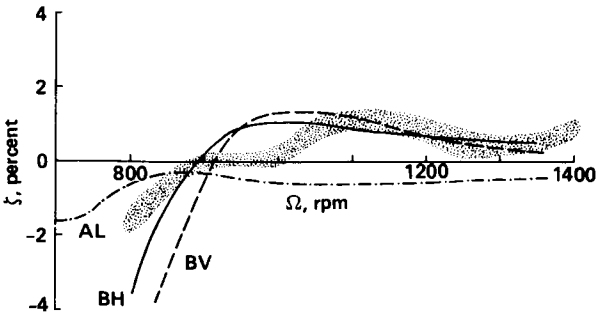

Fig. 4 Composite comparison of theory and experiment for Case 2, regressing lead-lag mode damping as a function of rotor speed for 1 g thrust; θ_{fh} = 0°, θ_{bf} = 9.6°, θ_{pc} = 0°, θ_{d} = 0°.

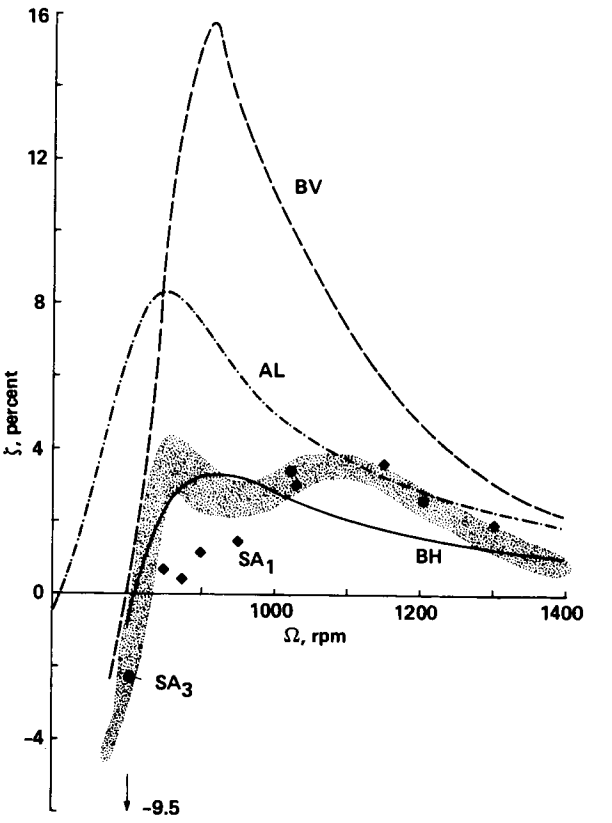

Fig. 5 Composite comparison of theory and experiment for Case 3, regressing lead-lag mode damping as a function of rotor speed for 1 g thrust; θ_{fh} = 12°, θ_{bf} = -2.4°, θ_{pc} = 0°, θ_{d} = -2.5°.

calculated to allow a valid assessment. The diamonds labeled SA_1 are results that were obtained by Sikorsky using the upgraded G400 analysis. When Sikorsky used their G400 analysis for this case during the contracted effort, the program would not converge. The upgraded analysis shows a substantial improvement, giving results between DRAV21 and the other codes.

The results for Case 4 are shown in Fig. 6. Unlike the other hover cases, the rotor speed was

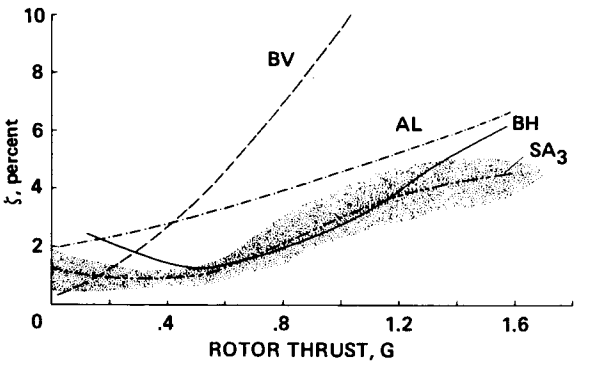

Fig. 6 Composite comparison of theory and experiment for Case 4, regressing lead-lag mode damping as a function of rotor speed for 1 g thrust; θ_{fh} = 12°, θ_{bf} = -2.4°, θ_{pc} = 0°, θ_{d} = -2.5°.

held constant and the rotor thrust was varied. The DRAV21 analysis shows good agreement with test data from about 0.5 to 1.2 g thrust. The lack of a proper stall representation in the aerodynamics representation is believed to be the reason for the differences seen above 1.2 g. Overall the correlation is considered to be fair to good. The C-90 analysis shows excessive sensitivity to the thrust or pitch angle and the agreement is judged as very poor to poor. The E927-3 analysis agrees quite well with the experimental results, so is considered good. The FLAIR analysis slightly overpredicts the damping level and shows similar trends, but is judged as only poor to fair.

The results of the comparison of the analyses with the three forward flight cases are shown in Figs. 7 through 9. For these cases, Bell Helicopter Textron used their C81 analysis (which was not used for the hover cases) and Boeing Vertol used their C-90 code. Sikorsky attempted to model the forward flight conditions using their E-927 analyses, but were unable to obtain stable solutions.

The results for Case 5, which show the lead-lag mode damping variation with wind tunnel speed, are shown in Fig. 7. The Bell Helicopter Textron C81 code shows good agreement with the data, both in behavior and in damping level. The Boeing Vertol C-90 analysis significantly overpredicts the damping level and the correlation is only considered to be very poor-to-poor. Sikorsky has provided a limited number of calculations with the upgraded G400 analysis. These results compare favorably with the test results.

Case 6 shows the lead-lag mode damping variation at one rotor speed and thrust as the shaft angle is varied to simulate climbs and descents. The predictions and experimental data are compared in Fig. 8. The Bell Helicopter Textron C81 prediction shows the correct damping level and damping behavior with shaft angle. The correlation is considered good. The Boeing Vertol damping is again significantly overpredicted, although the damping behavior with shaft angle is similar to the data. The correlation is judged to be poor.

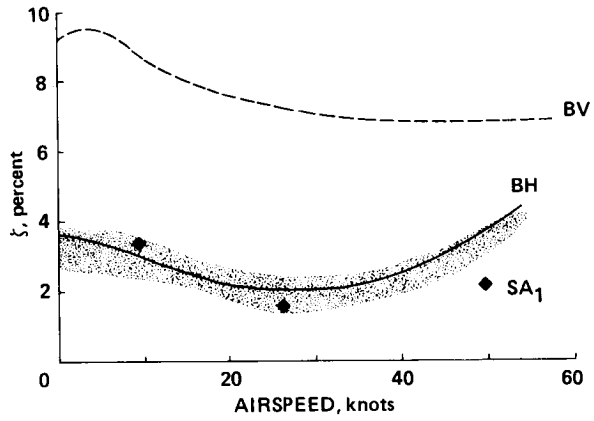

Fig. 7 Composite comparison of theory and experiment for Case 5, regressing lead-lag mode damping as a function of rotor speed for 1 g thrust; θ_{fh} = 12°, θ_{bf} = -2.4°, β_{pc} = 0°, β_d = -2.5°.

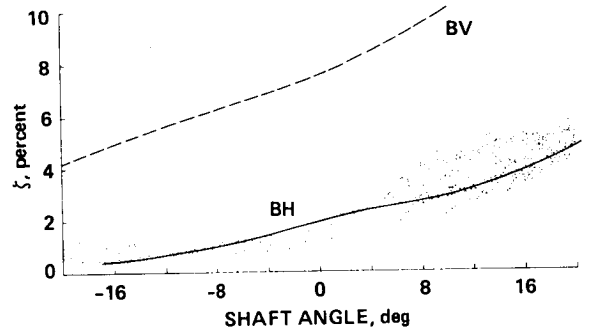

Fig. 8 Composite comparison of theory and experiment for Case 6, regressing lead-lag mode damping as a function of shaft angle for airspeed of 24.8 knots, 1 g thrust, and r = 1028 rpm; θ_{fh} = 12°, θ_{bf} = -2.4°, β_{pc} = 0°, β_d = -2.5°.

Figure 9 compares the measured and calculated lead-lag mode damping for Case 7 as rotor speed is varied at the minimum power speed. The damping behavior is very similar to the hover case that was shown in Fig. 5. The Bell Helicopter Textron C81 analysis shows approximately the same behavior as seen in the data, but the damping level tends to be lower and the neutral stability boundary is shifted downwards by about 40 rpm. The correlation is judged fair. The Boeing Vertol C-90 analysis also shows approximately correct behavior, but the damping level tends to be higher than the measured level. The neutral-stability rotor speed prediction is the same as for C81. Overall the correlation is considered poor-to-fair.

Conclusions

Five analyses were compared with one or more cases selected from an experiment that measured the frequency and damping of a model rotor in hover and in forward flight. The hover cases examined various couplings, while the forward flight case examined the effects of variations in

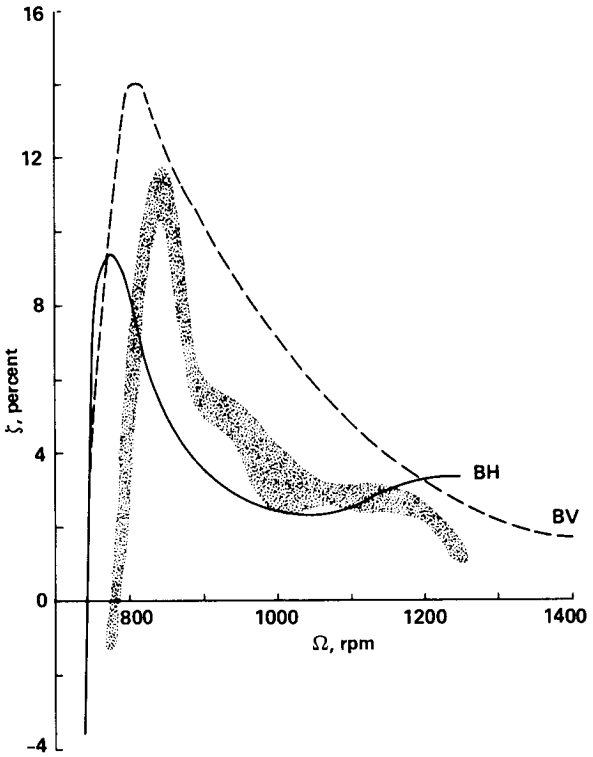

Fig. 9 Composite comparison of theory and experiment for Case 7, regressing lead-lag mode damping as a function of rotor speed for 1 g thrust and airspeed of 24.8 knots; θ_{fh} = 12°, θ_{bf} = -2.4°, β_{pc} = 0°, β_d = -2.5°.

forward speed, rotor speed, and shaft angle. Based on comparison of the analyses with the experimental data, the following conclusions were reached.

1) The DRAV21 analysis used by Bell Helicopter Textron gave fair-to-good correlation overall for the four hover cases. The C81 analysis used by Bell Helicopter Textron for the three forward-flight cases gave fair-to-good correlation overall.

2) The C-90 analysis used by Boeing Vertol to predict the stability for all of the cases gave poor-to-fair correlation.

3) Sikorsky Aircraft used the analysis codes G400 and E927-3 for the cases examined. The E927-3 code correlation for the hover cases shows mixed results. Limited calculations show very good agreement for two of the cases examined, but fail to adequately model precone in another hover case. Overall, the E927-3 was judged to give poor-to-fair correlation. The attempt to use the G400 analysis for the contracted effort gave unsatisfactory results. The program was upgraded later and some cases were run successfully. The calculations with the modified analysis show considerable improvement.

4) The Aeromechanics Laboratory FLAIR analysis provided poor-to-fair correlation overall.

References

[1]Chen, C., and Staley, J. A., "Aeroelastic Stability Test Results for a 1/5.86 Froude Scale Model of a Bearingless Main Rotor System on the BO 105 Helicopter," Boeing Vertol Company Rep. D210-11245-1, June 1977.

[2]Bousman, W. G., Sharpe, D. L., and Ormiston, R. A., "An Experimental Study of Techniques for Increasing the Lead-lag Damping of Soft Inplane Hingeless Rotors." Preprint No. 1035, American Helicopter Society 32nd Annual National Forum, May 1976.

Appendix A - Model Properties

The seven cases examined in this paper are from an experiment originally reported in Ref. 1. The experimental model properties in this appendix are taken from that reference.

To obtain the best representation of static and dynamic rotor aeroelastic characteristics of a full-scale helicopter, a Froude-scaled model was used. Froude scaling best maintains the proper relationship between dynamic, aerodynamic, elastic, and gravitational forces. Table 3 shows a comparison a full-scale, model-scale desired, and model-scale-actual parameters. The weight of the model was not scaled since the model had only pitch and roll degrees of freedom and only the inertias were scaled.

Rotor Properties

The rotor system tested in this experiment was a four-bladed bearingless system with a diameter of 5.5 ft which is 1/5.86 of full scale. The blades are untwisted with an NACA 23012 airfoil at the 1.65 in. chord width with an additional trailing edge tab of 0.17 in. Section lift and drag coefficient data for these blades have been calculated from steady-bending-moment data reported in a previous experiment (Ref. 2). Analytic functions that provide a good fit to these data are:

$$c_l = 0.15 + 5.73\alpha$$

$$c_d = 0.0079 + 0.17\alpha^2$$

$$c_{mo} = -0.012$$

where c_l is the section lift coefficient, α is the section angle of attack in radians, c_d is the section drag coefficient, and c_{mo} is the section moment coefficient. The camber of the NACA 23012 profile provides a section lift coefficient of 0.15 at zero pitch angle.

The beam and blade physical properties of weight, pitch inertia, flap bending EI, chord bending EI, and torsional rigidity versus blade radius are presented in Figs. 10 through 15. The

Table 3 Comparison of Full Scale and Model Properties

Parameter	Units	Model objective	Model actual	Full scale
Rotor diameter	ft	5.5	5.5	32.217
Rotor speed	rpm	1029	1029	425.0
Chord	in.	1.814	1.82	10.63
1st chord frequency	per rev	0.714	0.68	0.714
1st flap frequency	per rev	1.12	1.11	1.12
1st torsion frequency	per rev	3.66	4.45	3.66
Control system stiffness (nonrotating)	in.-lb/rad	31.9	37.8	37550.0
c.g.	% chord	25.1	24.35	25.0
a.c.	% chord	25.0	25.0	25.0
Precone (hub-beam)	deg	0	0, +2.5	0
Sweep (beam-blade)	deg	0	0, +2.5	0
Droop (beam-blade)	deg	0	0, -2.5	0
Hub and rotor weight	lbs	2.24	2.42	451.0
Pitch inertia w/rotor	lb-in.-sec^2	5.96	5.59	41174.0
Roll inertia w/rotor	lb-in.-sec^2	2.36	2.34	16304.0
Weight	lbs	22.4	38.8	4500.0

stiffness distribution of Fig. 10 is for a single beam only.

The control system stiffness of 0.664 in.-lb/deg is introduced at a blade radial station of 0.233R and includes the effects of the control system, torque tube, and flexbeam which

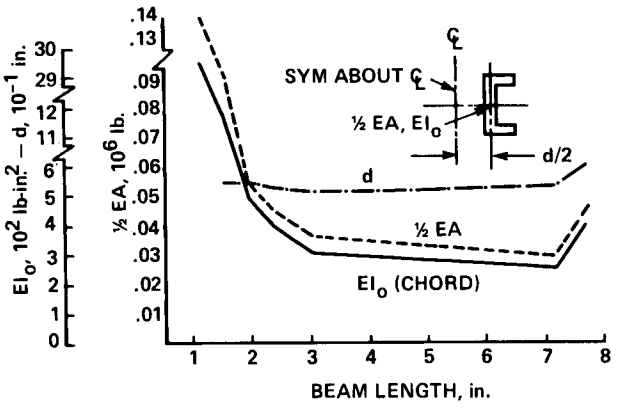

Fig. 10 Model beam chord properties; E = 0.6 × 10^6 lb/in.^{2}

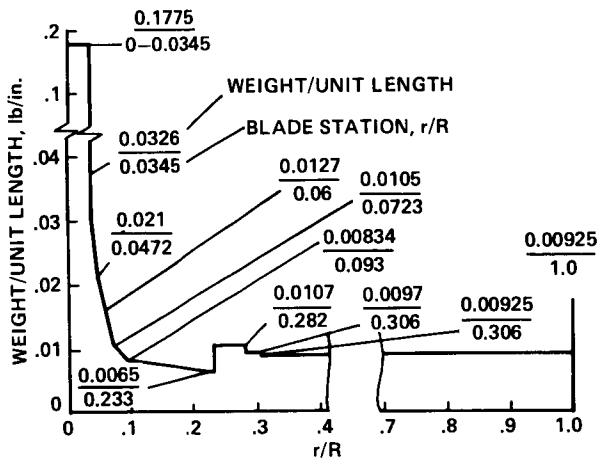

Fig. 11 Calculated model beam and blade weight/unit length (computed).

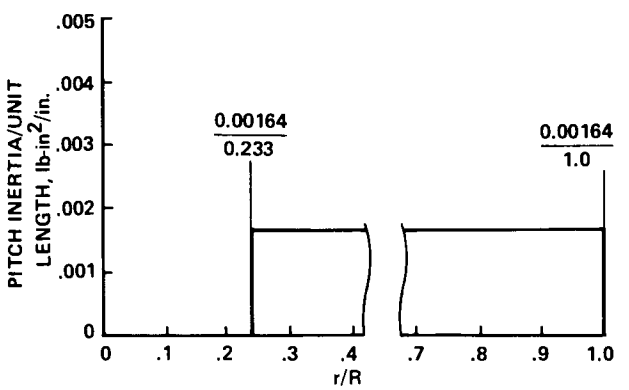

Fig. 12 Calculated model blade-pitch inertia per unit length (computed).

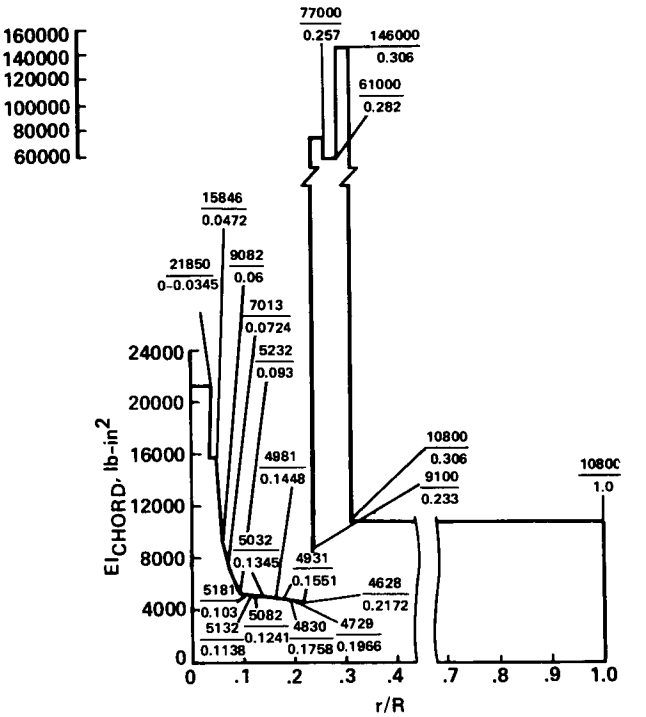

Fig. 13 Calculated model blade-chord stiffness.

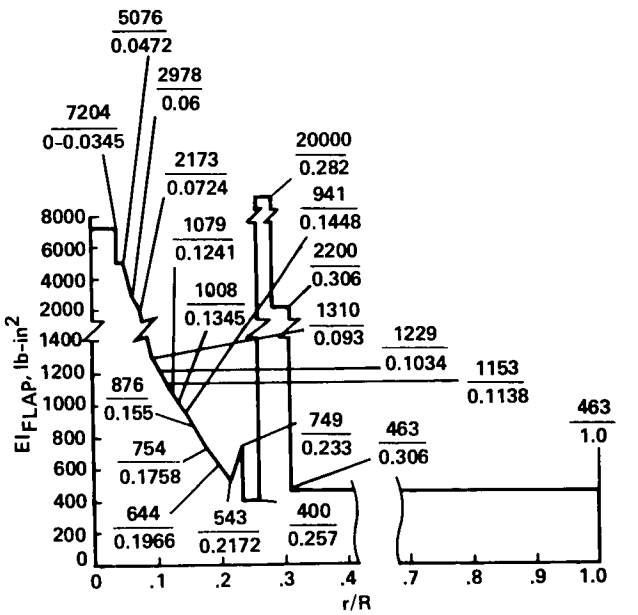

Fig. 14 Calculated model blade-flap stiffness.

were determined by twisting the blade at the flexbeam/blade attachment clevis (nonrotating). The effect of centrifugal stiffening is not included, but the calculated effect would be 0.07 in.-lb/deg at the nominal rotor speed. The torque tube is a 1/8-in. steel rod with a running mass of 0.00368 lb$_m$/in. and an EI of 360 lb-in.^{2} Its root end is pinned in flap but not chord. Figure 15 does not include the measured

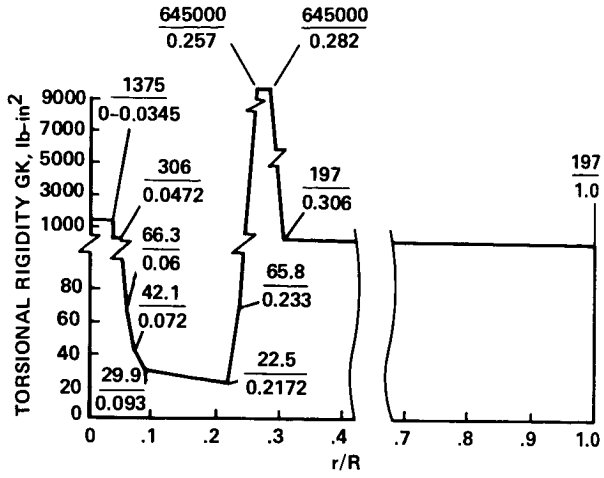

Fig. 15 Calculated model blade torsional rigidity.

model-control-system torsional stiffness of 0.664 in.-lb/deg.

Figure 16 shows a comparison between the frequencies of the 1/5.86 Froude-scaled rotor blade and the scaled-down values of the full-scale

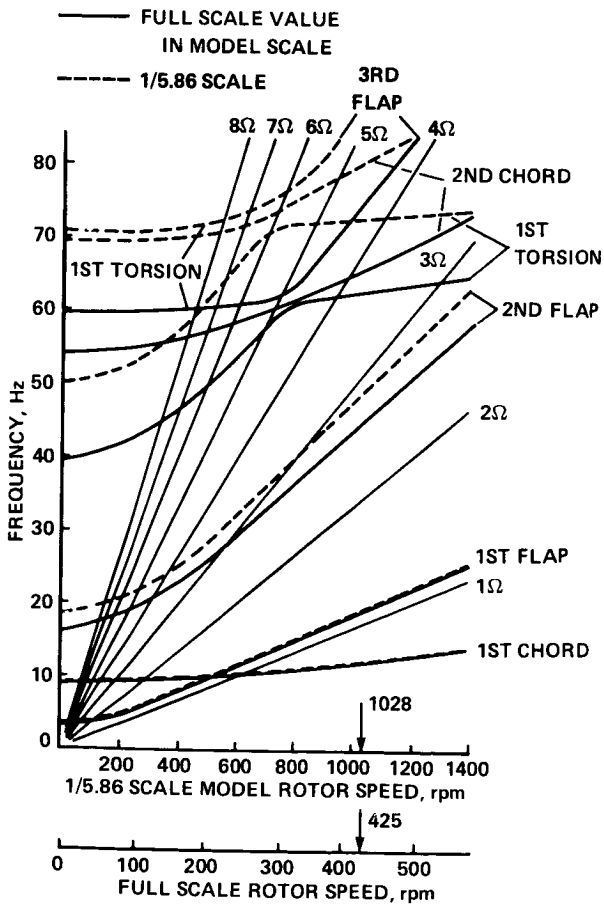

Fig. 16 Comparison of Froude Scale and corrected full-scale-model data.

BO 105 BMR. These frequencies were obtained from the Boeing Vertol Y-71 program, which is a fully coupled pitch/flap/lag analysis.

Body Properties

Prior to the aeroelastic stability testing in hover, several tests were made to determine the model fuselage inertia and damping properties. The model rigid-body inertia properties were measured with and without the rotor installed. The soft pitch and roll centering springs which center the body on the roll and pitch gimbal axes were temporarily replaced by stiffer springs so that the body roll and pitch frequencies could be determined accurately. The pitch-and-roll inertias were calculated from the nonrotating body natural frequencies and the known pitch-and-roll spring rates about the gimbal axes. The calculation for the body inertias used the following values: total rotor weight was 2.24 lb, height of the rotor above the pitch gimbal was 10.49 in., and blade flap inertia about the rotor center for one blade was 87 lb-in.^{2} Tables 4 and 5 present the results of these tests.

Appendix B - Experimental Data

The experimental data tabulated in this appendix were obtained from Ref. 1. Table 6 shows the regressing lead-lag mode damping for each test rotor speed for Case 1 at 1 g thrust in hover. This case corresponds to Fig. G-1 of Ref. 1. The data for Case 2 are shown in Table 7 and corresponds to Fig. G-18 of Ref. 1 and are also for 1 g thrust in hover. Table 8 shows the Case 3 data for 1 g thrust in hover and corresponds to Fig. G-26 of Ref. 1. The regressing lead-lag mode damping for Case 4 is shown in Table 9 for various values of thrust at a rotor speed of 1028 rpm in hover. This corresponds to Fig. G-28 of Ref. 1. Table 10 shows the lead-lag regressing damping in forward flight for various wind-tunnel-test speeds under 1 g thrust conditions for Case 5 which corresponds to Fig. G-72 of Ref. 1. The Case 6 data is shown in Table 11 which correspond to climb for positive shaft angles and descent for negative shaft angles. These data were obtained at the 24.8-knot test speed for 1-g thrust and a rotor speed of 1028 rpm. The data correspond to Fig. G-57 and G-71 of Ref. 1. Table 12 shows the lead-lag regressing mode damping as a function of rotor speed at a tunnel speed of 24.8 knots and 1 g thrust. This Case-7 condition corresponds to Fig. G-39 of Ref. 1.

Appendix C - Correlation

All of the theoretical predictions and experimental data are shown in this appendix in Figs. 17-30. In some cases figures from the main text are repeated here for completeness. Two formats are used for the correlation. The first format compares the theoretical predictions and

Table 4 Fuselage Pitch Inertia and Damping (Nonrotating)

Parameter	Model value
Pitch spring rate (stiff), in.-lb/rad	3900.0
Pitch spring rate (soft), in.-lb/rad	272.0
Body pitch frequency (without rotor--stiff spring), Hz	4.68
Body pitch frequency (with rotor--stiff spring), Hz	4.14
Body pitch frequency (with rotor--soft spring), Hz	1.11
Body pitch damping (stiff spring), percent critical	6.64
Body pitch damping (soft spring), percent critical	7.18
Body pitch inertia (without rotor, frequency = 4.68 Hz), lb-in.^{2}	1741.0
Total pitch inertia (with rotor, frequency = 6.68 Hz), lb-in.^{2}	2157.0
Total pitch inertia (with rotor, frequency = 4.14 Hz), lb-in.^{2}	2224.0

Table 5 Fuselage Roll Inertia and Damping (Nonrotating)

Parameter	Value
Roll spring rate (stiff), in.-lb/rad	1193.0
Roll spring rate (soft), in.-lb/rad	195.0
Body roll frequency (without rotor--stiff spring), Hz	4.90
Body roll frequency (with rotor--stiff spring), Hz	3.53
Body roll frequency (with rotor--soft spring), Hz	1.29
Body roll damping (stiff spring), percent critical	5.68
Body roll damping (soft spring), percent critical	2.29
Body roll inertia (without rotor, frequency = 4.9 Hz), lb-in.^{2}	486.0
Total roll inertia (with rotor, frequency = 4.9 hz), lb-in.^{2}	902.0
Total roll inertia (with rotor, frequency = 3.53 Hz), lb-in.^{2}	936.0

Table 6 Case 1 Modal Damping

Ω, rpm	ζ_r, %
825	-2.1
850	0.1
875	0.5
900	0.65
925	0.9
950	1.15
1000	1.7
1028	2.1
1050	2.1
1100	2.5
1125	2.2
1200	1.2
1250	0.8

Table 7 Case 2 Modal Damping

Ω, rpm	ζ_r, %
800	-1.7
850	0.5
900	0.0
950	0.0
975	0.0
1000	0.1
1028	0.55
1050	0.95
1100	1.1
1150	1.1
1200	0.9
1250	0.25
1250	0.65
1300	0.5
1350	0.5
1400	0.85

Table 8 Case 3 Modal Damping

Ω, rpm	ζ_r, %
775	-4.35
800	2.3
825	0.1
825	0.9
850	3.7
850	4.2
875	3.5
900	3.5
900	2.4
925	2.7
950	2.3
1000	2.7
1000	3.25
1028	3.15
1028	3.7
1100	3.75
1150	3.3
1200	2.7
1250	1.95
1300	1.90
1350	1.1
1400	0.8

Table 9 Case 4 Modal Damping

Thrust, g	ζ_r, %
0.0	0.6
0.0	1.75
0.14	0.65
0.14	1.4
0.33	0.7
0.33	0.9
0.58	0.9
0.58	1.3
0.87	1.85
0.87	3.3
1.00	3.15
1.00	3.7
1.13	2.8
1.13	4.45
1.46	3.55
1.46	4.9
1.7	4.55

Table 10 Case 5 Modal Damping

V, ft/sec	ζ_r, %
8.3	2.55
8.3	3.5
16.5	2.15
16.5	2.4
24.8	1.5
24.8	2.3
33.0	2.0
33.0	2.0
41.3	2.7
41.3	2.8
45.4	2.55
45.4	2.6
49.6	3.25
49.6	3.25
49.6	3.6
53.7	3.9
53.7	4.1

Table 11 Case 6
Modal Damping

α_s, deg	ζ_r, %
-20.5	0.45
-20.5	0.55
-20.1	0.95
-20.1	1.1
-15.1	0.9
-15.1	1.1
-15.1	0.5
-15.1	0.6
-11.1	1.15
-11.1	1.15
-9.9	0.6
-9.9	0.6
-4.9	0.85
-4.9	0.85
-4.8	1.15
-0.4	1.15
-0.4	1.0
0.3	1.1
0.3	1.7
5.0	1.7
5.0	2.9
5.0	3.1
5.0	1.75
10.0	1.9
10.0	4.55
10.0	4.7
10.0	2.3
14.5	2.45
14.5	3.1
15.1	3.3
15.1	4.85
19.4	5.15
19.4	4.25
20.0	4.4
20.0	5.1
	5.65

Table 12 Case 7
Modal Damping

Ω, rpm	ζ_r, %
775	-1.15
800	4.1
800	5.1
850	11.6
900	5.95
900	5.35
950	4.5
950	5.2
1000	2.6
1000	2.9
1028	3.4
1028	3.55
1050	2.75
1050	3.1
1100	2.6
1100	2.95
1150	2.5
1150	2.9
1200	2.3
1200	2.45
1250	1.1
1250	1.25

experimental data individually for each mathematical model used. In this format the actual calculated points are shown as solid symbols and the fairing between points calculated by the experiment analysts is indicated by open symbols. The second format compares all the theoretical predictions on a single composite plot using the faired curve from the first format and the experimental data are shown as a stippled area. A code is used to identify the theoretical predictions for both the individual and composite comparisons and is explained in Table 13.

Table 13 Explanation of Prediction Codes

ID	Prediction method	User
BH	DRAV21 (hover) C81 (forward flight)	Bell Helicopter Textron
BV	C-90	Boeing Vertol
SA_1	G400	Sikorsky Aircraft
SA_3	E927-3	Sikorsky Aircraft
AL	FLAIR	U.S. Army Aeromechanics Laboratory

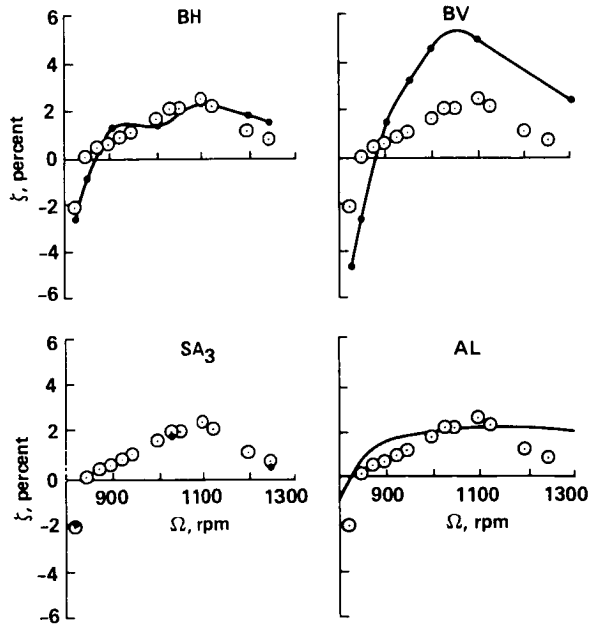

Fig. 17 Individual comparison for Case 1, regressing lead-lag mode damping as a function of rotor speed.

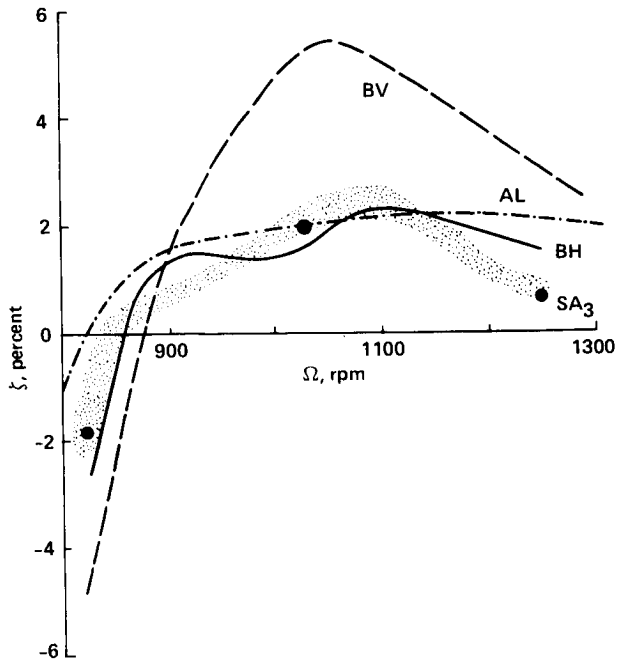

Fig. 18 Composite comparison for Case 1, regressing lead-lag mode damping as a function of rotor speed.

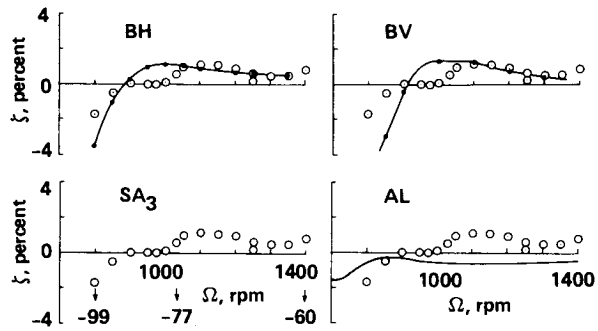

Fig. 19 Individual comparison for Case 2, regressing lead-lag mode damping as a function of rotor speed.

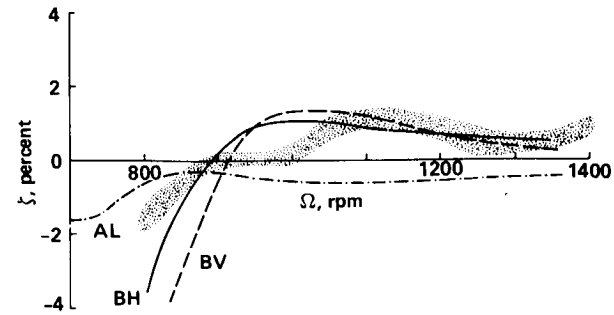

Fig. 20 Composite comparison for Case 2, regressing lead-lag mode damping as a function of rotor speed.

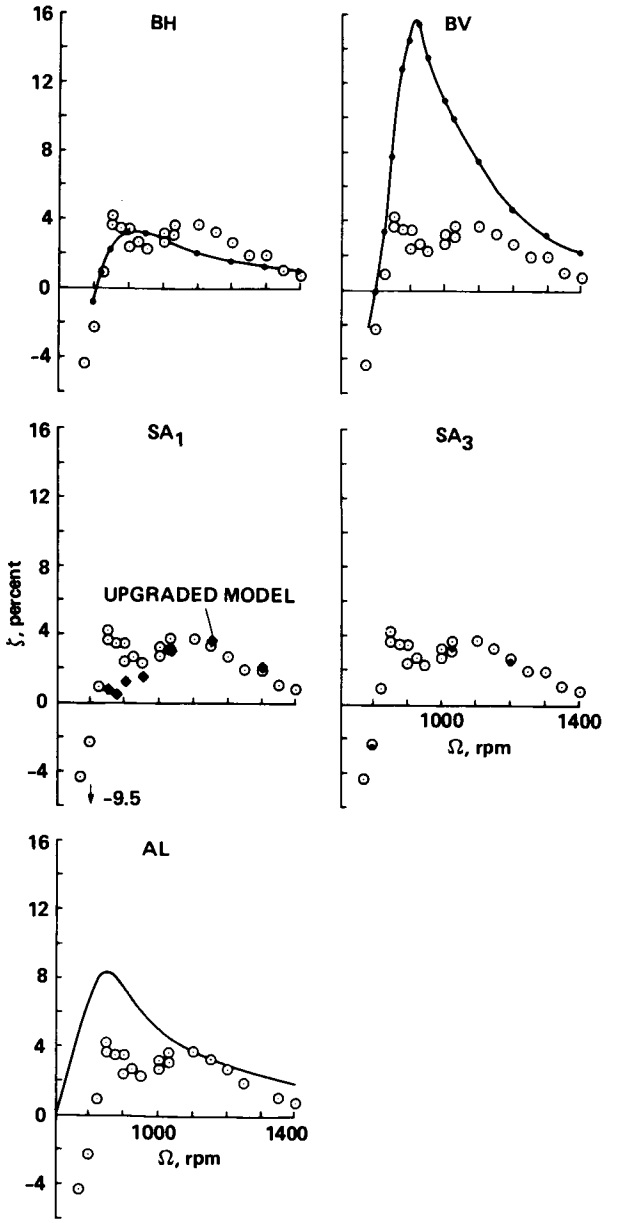

Fig. 21 Individual comparison for Case 3, regressing lead-lag mode damping as a function of rotor speed.

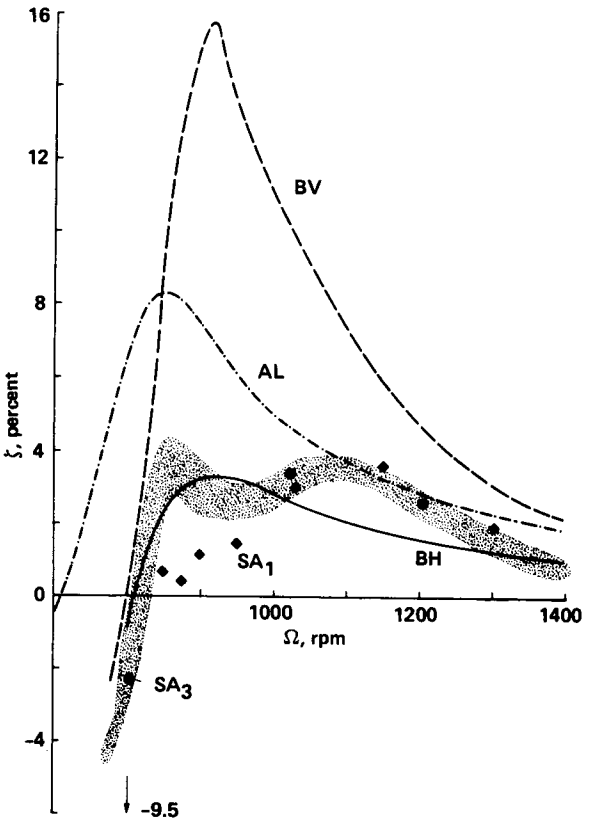

Fig. 22 Composite comparison for Case 3, regressing lead-lag mode damping as a function of rotor speed.

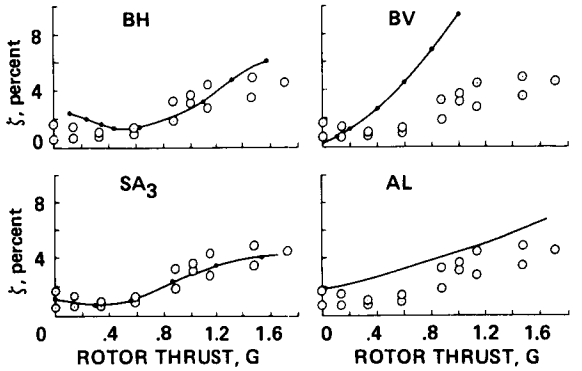

Fig. 23 Individual comparison for Case 4, regressing lead-lag mode damping as a function of rotor speed.

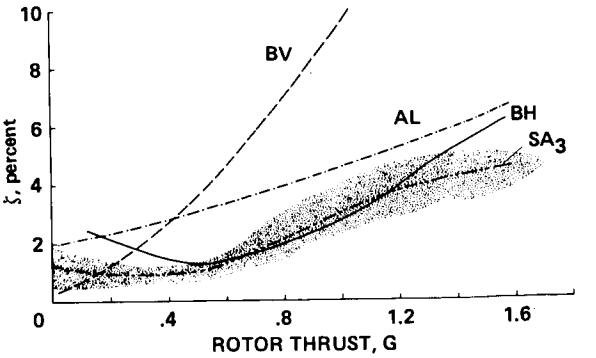

Fig. 24 Composite comparison for Case 4, regressing lead-lag mode damping as a function of rotor speed.

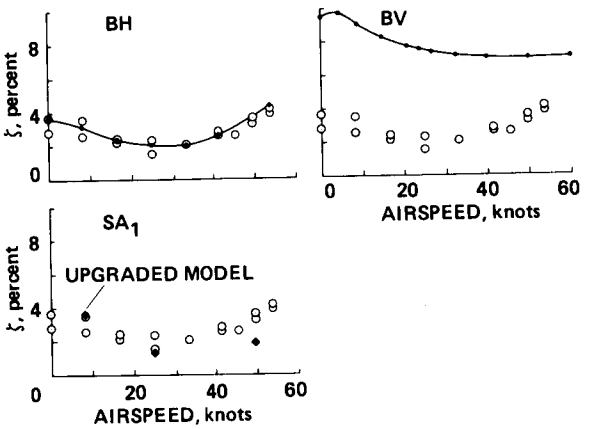

Fig. 25 Individual comparison for Case 5, regressing lead-lag mode damping as a function of rotor speed.

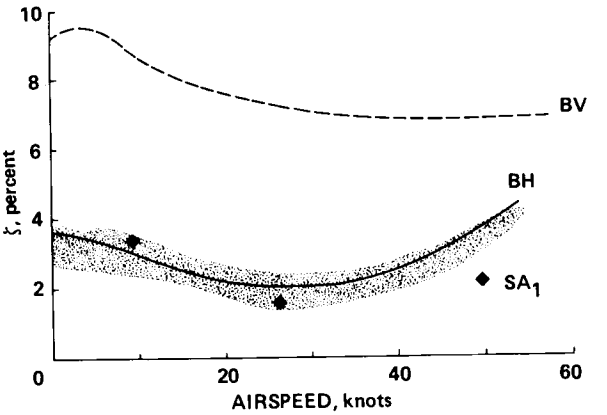

Fig. 26 Composite comparison for Case 5, regressing lead-lag mode damping as a function of rotor speed.

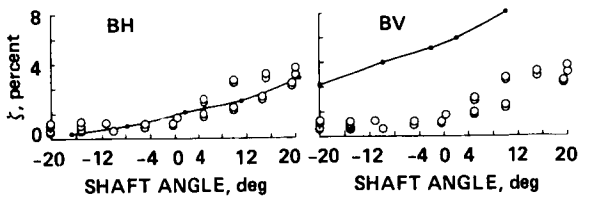

Fig. 27 Individual comparison for Case 6, regressing lead-lag mode damping as a function of shaft angle.

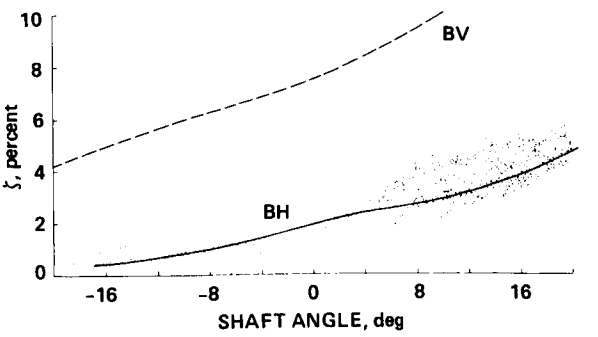

Fig. 28 Composite comparison for Case 6, regressing lead-lag mode damping as a function of shaft angle.

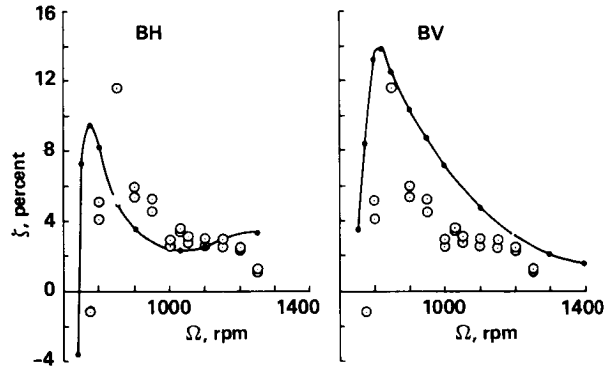

Fig. 29 Individual comparison for Case 7, regressing lead-lag mode damping as a function of rotor speed.

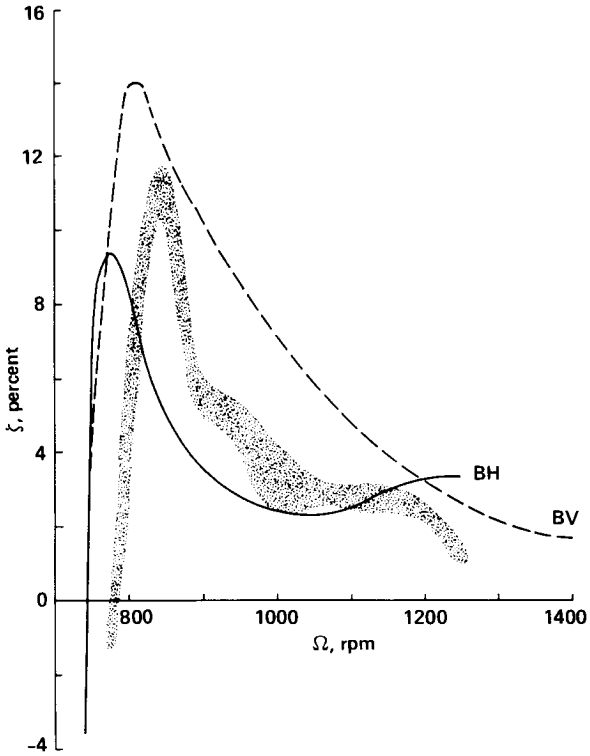

Fig. 30 Composite comparison for Case 7, regressing lead-lag mode damping as a function of rotor speed.